1-2005

Numerical Simulation of Double-Diffusive Finger Convection

Joseph D. Hughes
University of South Florida

Ward E. Sanford
USGS

H. L. Vacher
University of South Florida, vacher@usf.edu

Numerical simulation of double-diffusive finger convection

Joseph D. Hughes
Department of Geology, University of South Florida, Tampa, Florida, USA

Ward E. Sanford
U.S. Geological Survey, Reston, Virginia, USA

H. Leonard Vacher
Department of Geology, University of South Florida, Tampa, Florida, USA

Received 17 October 2003; revised 30 April 2004; accepted 7 October 2004; published 29 January 2005.

[1] A hybrid finite element, integrated finite difference numerical model is developed for the simulation of double-diffusive and multicomponent flow in two and three dimensions. The model is based on a multidimensional, density-dependent, saturated-unsaturated transport model (SUTRA), which uses one governing equation for fluid flow and another for solute transport. The solute-transport equation is applied sequentially to each simulated species. Density coupling of the flow and solute-transport equations is accounted for and handled using a sequential implicit Picard iterative scheme. High-resolution data from a double-diffusive Hele-Shaw experiment, initially in a density-stable configuration, is used to verify the numerical model. The temporal and spatial evolution of simulated double-diffusive convection is in good agreement with experimental results. Numerical results are very sensitive to discretization and correspond closest to experimental results when element sizes adequately define the spatial resolution of observed fingering. Numerical results also indicate that differences in the molecular diffusivity of sodium chloride and the dye used to visualize experimental sodium chloride concentrations are significant and cause inaccurate mapping of sodium chloride concentrations by the dye, especially at late times. As a result of reduced diffusion, simulated dye fingers are better defined than simulated sodium chloride fingers and exhibit more vertical mass transfer.

Citation: Hughes, J. D., W. E. Sanford, and H. L. Vacher (2005), Numerical simulation of double-diffusive finger convection, *Water Resour. Res.*, *41*, W01019, doi:10.1029/2003WR002777.

1. Introduction

[2] A wide range of convective structures resulting from local hydrodynamic instabilities can develop in fluids containing multiple species that affect fluid density and viscosity. Convection can occur in systems that are initially in density-stable configurations and contain two or more components with different diffusivities that make opposing contributions to vertical density gradients. Diffusivity differences can result in buoyant instabilities capable of initiating convection. The nature of the convective flow is strongly dependent on the initial distribution and concentration of each component. In cases when the lower-diffusivity component is on top, a parcel of fluid perturbed downward across the interface takes on solute mass from the surrounding fluid faster that it diffuses solute mass so the parcel continues to fall. This mode of convection is termed double-diffusive or multicomponent finger convection and is characterized by convection driven by long, narrow columns (fingers) of rising and falling fluid. Alternatively, when the higher diffusivity component is on top, a parcel of fluid perturbed downward across the interface diffuses mass outward to the surrounding fluid more rapidly than it gains mass from the lower-diffusivity solute. The parcel of fluid then becomes less dense than the surrounding fluid, moves upward, and overshoots its original position before repeating the motion. This mode of convection is termed oscillatory double-diffusive convection and can lead to well-mixed convecting layers separated by sharp contrasts in fluid density. Convection features are much different from those that develop in stable advective, dispersive, and/or diffusive processes, and can significantly increase mass transfer rates. Double-diffusive or multicomponent finger convection is an important mixing process in the open ocean and can be an important process in contaminant transport in porous media [*Green*, 1984; *Imhoff and Green*, 1988; *Cooper et al.*, 1997].

[3] Laboratory methods used to quantify convective systems have ranged from intrusive methods that sample portions of the developing convective system [e.g., *Turner*, 1967; *Imhoff and Green*, 1988] to nonintrusive optical methods [e.g., *Lambert and Demenkow*, 1971; *Kazmierczak*

0043-1397/05/2003WR002777

and Poulikakos, 1989]. These experimental methods have increased understanding of double-diffusive and multicomponent processes but have not been used directly in numerical simulations because of the limited amount of data collected in typical Hele-Shaw experiments.

[4] Recent application of nonintrusive light transmission techniques to double-diffusive Hele-Shaw experiments has allowed collection of point-wise concentration measurements over entire flow fields at relatively high spatial ($\sim$0.015 cm) and temporal (<1 s) resolution [e.g., *Cooper et al.*, 1997, 2001; *Pringle et al.*, 2002]. These experiments have investigated double-diffusive flow field evolution for systems with different initial departures from equilibrium and have increased understanding of double-diffusive processes by allowing full-field determination of fluid mass transfer rates and the temporal evolution of fluid mass transfer. Additionally, these high-resolution data sets are ideal for comparison with numerical models capable of simulating double-diffusive flow processes.

[5] In this study, experimental Hele-Shaw results collected by *Pringle et al.* [2002] using nonintrusive light transmission techniques are used to verify a variable-density and variable-viscosity numerical code (based on SUTRA [*Voss and Provost*, 2002]) capable of simulating multicomponent variable-density fluid flow and transport [*Hughes and Sanford*, 2004]. The data set of *Pringle et al.* [2002] is well-suited for code verification of double-diffusive and multicomponent flow and transport numerical models because, unlike most previous experimental Hele-Shaw data sets, it is of sufficient spatial and temporal resolution to allow accurate comparisons of simulated and observed convective fingering. In some cases, when an appropriate observed data set was unavailable, numerical codes have been tested against other numerical codes. Consistent model results were often considered sufficient to demonstrate that a numerical code accurately represents the physics of a given problem. Verification of the numerical code presented in this paper would have been difficult without the data set of *Pringle et al.* [2002] because no generic numerical codes capable of simulating double-diffusive and multicomponent flow and transport in porous media are widely available [*Sorak and Pinder*, 1999].

[6] Hele-Shaw experiments are appropriate for verification of variable-density numerical codes because they evolve in response to internal conditions and are not forced by external boundary conditions. Dependence of many "standard" variable-density test cases on external boundary conditions often reduces the ability to isolate numerical inadequacies [*Voss and Souza*, 1987].

[7] In addition, the spatial and temporal resolution of the data of *Pringle et al.* [2002] is sufficient to improve our understanding of simulating nonlinear fingering processes. The full-field images from the experimental data set allow qualitative comparison of the evolving flow field and quantitative comparison of mass transfer rates. The ability to compare mass transfer rates allows the level of discretization required to accurately simulate nonlinear fingering and the mass transfer rates of each component to be evaluated.

2. Governing Equations

[8] The mass balance of fluid per unit aquifer volume, assuming fully saturated flow and negligible contribution of solute dispersion to the mass average flux of the fluid, is given by *Bear* [1979]:

$$(\rho((1-\varepsilon)\alpha+\varepsilon\beta))\frac{\partial p}{\partial t}+\varepsilon\left(\sum_{k=1}^{NS}\frac{\partial \rho}{\partial C_k}\frac{\partial C_k}{\partial t}\right) - \nabla\cdot\left[\left(\frac{\mathbf{k}\rho}{\mu}\right)\cdot(\nabla p-\rho\mathbf{g})\right]=Q_p \quad (1)$$

where

ρ(x, y, z, t)	the fluid density [M/L^3];
ε(x, y, z)	the effective porosity (dimensionless);
α	the compressibility of the porous matrix [M/LT^2]$^{-1}$;
β	the compressibility of the fluid [M/LT^2]$^{-1}$;
p(x, y, z, t)	the fluid pressure [M/LT^2];
NS	the number of dissolved species simulated;
C_k(x, y, z, t)	the solute concentration of species k [M$_{solute}$/M$_{fluid}$];
$\mathbf{k}$(x, y, z)	the intrinsic permeability tensor [L^2];
μ(x, y, z, t)	the fluid viscosity [M/LT];
$\mathbf{g}$	the gravitational acceleration vector [L/T^2];
Q_p(x, y, z, t)	a fluid mass source [M/L^{3}T].

[9] Fluid density is approximated as a linear function of solute concentration, expressed as

$$\rho=\rho_o+\sum_{k=1}^{NS}\frac{\partial\rho}{\partial C_k}(C_k-C_{ko}) \quad (2)$$

where ρ_o is the fluid density at the base concentration of all simulated species; C_{ko} is the base solute mass fraction of species k; and $\partial\rho/\partial C_k$ is a constant coefficient of density variability for each species. Fluid viscosity is approximated as a linear function of solute concentration:

$$\mu=\mu_o+\sum_{k=1}^{NS}\frac{\partial\mu}{\partial C_k}(C_k-C_{ko}) \quad (3)$$

where μ_o is the fluid viscosity at the base concentration of all simulated species; C_{ko} is the base solute mass fraction of species k; and $\partial\mu/\partial C_k$ is a constant coefficient of viscosity variability for each species.

[10] Darcy's law gives the average fluid velocity at a point as

$$\mathbf{v}=-\left(\frac{\mathbf{k}}{\varepsilon\mu}\right)\cdot(\nabla p-\rho\mathbf{g}) \quad (4)$$

[11] The solute mass balance per unit volume of a variable density fluid containing more than one dissolved species that may affect density is given by *Bear* [1979]:

$$\varepsilon\rho\frac{\partial C}{\partial t}+\varepsilon\rho\mathbf{v}\cdot\nabla C-\nabla\cdot[\varepsilon\rho(D_{mk}\mathbf{I}+\mathbf{D}_k)\cdot\nabla C]=Q_p(C_k^*-C_k) \quad (5)$$

where

$\mathbf{v}$(x, y, z, t)	the fluid velocity [L/T];
D_{mk}	the molecular diffusivity of species k, [L^2/T];

Table 1. Hele-Shaw Cell Experiment Parameters

Parameter	Value
Length L	0.2541 m
Height H	0.1625 m
Cell angle relative to horizontal	25°
Light acquisition data points	1650 pixels × 1055 pixels
Pixel size	1.54×10^{-4} m
Aperture width $\langle b \rangle$	1.77×10^{-4} m
Intrinsic permeability k	2.61×10^{-9} m^2

$\mathbf{I}$	the identity tensor;
$\mathbf{D}_k$(x, y, z, t)	the mechanical dispersion tensor of species k, [L^2/T];
C_k^*(x, y, z, t)	the solute concentration of the source fluid of species k, [M_{solute}/M_{fluid}].

[12] A generalized version of mechanical dispersion in isotropic homogeneous porous media is used to account for dispersion in an anisotropic porous medium. A detailed description of the generalized mechanical dispersion model used is given by *Voss and Provost* [2002].

3. Numerical Approximation

[13] The basic framework of the code to approximate equations (1) and (5) is based on a version of SUTRA capable of simulating two- and three-dimensional problems [*Hughes and Sanford*, 2004]. Equations (1) and (5) are approximated using a weighted numerical-residual method that combines Galerkin finite element and integrated finite difference techniques. Time derivative and source terms in equations (1) and (5) are discretized cell-wise and all other terms are discretized element-wise.

[14] The Galerkin finite element method allows geometric flexibility in mesh design and gives robust direction- and anisotropy-independent representation of fluid and solute fluxes. The integrated finite difference representation for the spatial integration of all nonflux terms in the governing equations provides an economical alternative to the Galerkin method while giving accuracy sufficient for any mildly nonlinear simulation problem.

[15] The hybrid weighted-residual and integrated finite difference method applied to the fluid mass balance (1) and solute mass balance for each species (5) is discussed in Appendix A.

4. Experimental Double-Diffusive Hele-Shaw Study of *Pringle et al.* [2002]

[16] *Pringle et al.* [2002] used a Hele-Shaw cell to explore the temporal and spatial distribution of double-diffusive finger convection of two fluids initially in a density-stable configuration with a mean interface thickness of $\sim 1 \times 10^{-3}$ m. The evolution of the resulting convection system was monitored using a quantitative light transmission technique. This quantitative light transmission technique allowed acquisition of full-field concentration data at a spatial and temporal resolution of 1.54×10^4 m and 1 second, respectively. Full details of the experimental procedure are given by *Pringle et al.* [2002]. The relevant features of the experiment are briefly discussed here and form the basis of the present numerical study.

[17] The mean aperture width ($\langle b \rangle$) of the Hele-Shaw cell was 1.77×10^{-4} m. Other relevant physical properties of the Hele-Shaw cell are given in Table 1. The equivalent intrinsic permeability (k) is 2.61×10^{-9} m^2 based on the relationship $k = \langle b \rangle^2/12$ [*Bear*, 1988]. The Hele-Shaw cell was filled with a sucrose solution (S) over a sodium chloride solution (T). The fluid properties of the sucrose and sodium chloride solutions are given in Table 2.

[18] The dimensionless buoyancy ratio, $R\rho = \beta_T \Delta T/\beta_S \Delta S$, is near neutral gravitational stability at 1.22, where ΔT is the maximum initial sodium chloride concentration, ΔS is the maximum initial sucrose concentration, $\beta_T = -(1/\rho_o)(\partial\rho/\partial T)$ and $\beta_S = -(1/\rho_o)(\partial\rho/\partial S)$ are the concentration expansion coefficients [*Nield and Bejan*, 1998] of sodium chloride and sucrose, respectively. The dimensionless solutal Rayleigh numbers, with permeability included in the scaling of viscous influences, are defined as $R_T = \beta_T \Delta T g H k/D_T \nu$ and $R_S = \beta_S \Delta S g H k/D_S \nu$, where g is the gravitational acceleration in the plane of the cell, H is the cell height, k is the intrinsic permeability, D_T is the molecular diffusivity of sodium chloride, D_S is the molecular diffusivity of sucrose, and ν is the mean kinematic viscosity of the fluid. The Hele-Shaw cell was inclined at an angle of 25° relative to horizontal and gravitational acceleration in the plane of the cell is 4.14 m/s^2 based on $\mathbf{g}\sin\theta$. The location of the Hele-Shaw experiment in Rayleigh parameter space is shown in Figure 1.

[19] To visualize sodium chloride concentrations and quantify convective motion, a dye tracer with a concentration of 0.00025 kg/kg was mixed with the sodium chloride solution. The dye had a negligible effect on fluid density. Sodium chloride concentrations are not mapped perfectly by the dye because the diffusivity of sodium chloride is approximately 2.5 times greater than the diffusivity of the dye (Table 2). Because the motion is convective through most of the experiment, *Pringle et al.* [2002] suggested the diffusivity differences had little impact on the mapping of sodium chloride concentrations over the length of time of the experiment.

[20] To minimize initial perturbations, the inclined Hele-Shaw cell was initially saturated with water, then the sucrose and sodium chloride-dye solutions were flushed through the cell at the upper and lower corners of one side, respectively, and flushed out of the center at the opposite

Table 2. Fluid Properties and Rayleigh Numbers

Parameter	Value
ΔT^a	0.03463 (kg_{solute}/kg_{fluid})
ΔS^b	0.05234 (kg_{solute}/kg_{fluid})
ΔDye	0.00025 (kg_{solute}/kg_{fluid})
β_T	−0.6892 (kg/kg)
β_S	−0.3719 (kg/kg)
D_T	1.477×10^{-9} m^2 s^{-1}
D_S	4.878×10^{-10} m^2 s^{-1}
$D_{dye}{}^c$	5.670×10^{-10} m^2 s^{-1}
ν_T	1.033×10^{-6} m^2 s^{-1}
ν_S	1.125×10^{-6} m^2 s^{-1}
R_T	26,460
R_S	21,579

[a] T and subscript T used to denote sodium chloride.
[b] S and subscript S used to denote sucrose.
[c] From *Detwiler et al.* [2000].

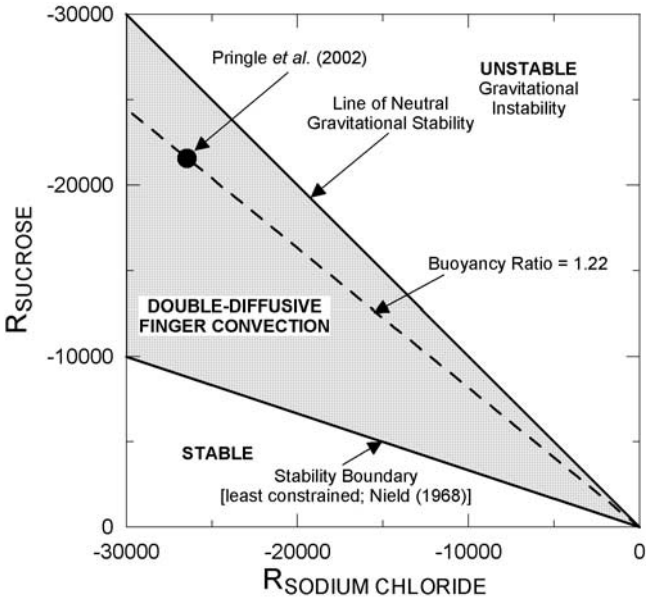

Figure 1. Location of the Hele-Shaw experiment (solid circle) within Rayleigh parameter space with an R_ρ value of 1.22.

side. After ~100 Hele-Shaw cell volumes of each fluid were flushed, the inflow and outflow valves were closed, and the instability was allowed to evolve naturally from the rest state. *Pringle et al.* [2002] presented images of the flushing process and concentrations prior to initiating of the experiment that indicated the upper and lower portions of the Hele-Shaw cell contained sucrose and sodium chloride in an initially stratified configuration, respectively, and the interface was free of discernable perturbations. The initial solution interface had a mean thickness of ~0.001 m and was determined by single pixel-wide vertical transects across the cell. Minimization of artificial perturbations is important because these perturbations can influence fluid motion and make interpretation of experimental data difficult.

[21] Light images were transformed by *Pringle et al.* [2002] into normalized concentration fields (C/C_o) using calibration curves developed using solutions of known dye and sodium chloride concentrations. Normalized concentrations (C/C_o) are referred to as "concentration" in the remainder of the paper.

[22] A total of 300 images of the evolving concentration field were collected over the duration of the 16-hour Hele-Shaw experiment. Images were collected at 20-s intervals during early times and at 10-min intervals at late times. A sequence of concentration fields from the experiment is shown in Figure 2 and was chosen by *Pringle et al.* [2002] because the images captured upward mass transfer of sodium chloride and evolution of the convection system during the early, mature, and rundown stages of the experiment. Time is presented as dimensionless ($t^* = tD_T/H^2$) based on the dimensionless governing equations of *Nield and Bejan* [1998].

[23] Starting from the rest state, distinct fingers develop quickly and grow rapidly in unison. As convection proceeds, small-scale fingers continuously develop from the region of the initial solution interface. The complexity of the fingers increases after t^* of 2.21×10^{-4} (Figure 2c) and includes coalescing of fingers and generation of new finger pairs at the tips of some upward and downward growing fingers. At t^* of 4.23×10^{-4} (Figure 2e) the fastest growing fingers reach the top and bottom boundaries of the cell and begin to spread laterally forming more and less dense plumes of fluid at the bottom and top of the cell, respectively. The plumes migrate to the center of the upper and lower boundary in Figures 2f–2h, and new fingers continue to form at the initial solution interface located at the centerline in regions with near-initial fluid concentrations. At late times, the finger structure exhibits a branching pattern with greater lateral travel than observed at early times. Diffusion begins to dominate the flow field at late times which slowly begins to decrease spatial variations in fluid concentrations and results in a well mixed concentration field at $t^* > 1.77 \times 10^{-3}$.

5. Numerical Modeling

5.1. Spatial Discretization and Model Parameters

[24] The Hele-Shaw cell was discretized using 671,744 elements. A uniform mesh, with square elements 2.48×10^{-4} m along each side, was used throughout the model domain. A uniform mesh was used because convection did not appear to occur in preferential locations during the original Hele-Shaw experiment.

[25] Transport of sodium chloride, sucrose, and the dye was simulated along with fluid flow. The relationship of fluid density and viscosity to sodium chloride and sucrose concentrations was developed from data of *Weast* [1986]. Fluid density and viscosity are approximately linearly related to sodium chloride and sucrose concentrations over the range of concentrations used in the Hele-Shaw experiments (Table 2) as shown in Figure 3. The coefficient of determination (R^2) for linear regression of all sodium chloride and sucrose concentration-density and concentration-viscosity data was greater than 0.99 (Figure 3). The effects of sodium chloride and sucrose concentrations on fluid density and viscosity were assumed to be independent of each other and additive (equations (2) and (3)). Dye concentrations were assumed to have no effect on fluid density or viscosity. Except for dispersion in the flow direction resulting from nonuniform velocity profiles across the width of the Hele-Shaw cell (Taylor dispersion), which is not represented in the numerical model and is typically less than molecular diffusion [*Detwiler et al.*, 2000], mechanical dispersion does not occur in a Hele-Shaw cell. As a result, longitudinal and transverse dispersivities were set to zero and molecular diffusion was the only dispersive component simulated. Additional flow and solute transport parameters are summarized in Tables 2 and 3.

5.2. Boundary and Initial Conditions

[26] No-flux conditions were assumed at all external boundary faces except the upper left and right corners of the Hele-Shaw cell. Specified pressure boundary conditions with a pressure of 0.00 Pa and associated sodium chloride and dye concentrations of 0.0 kg/kg and sucrose concentrations of 0.05234 kg/kg were assigned at the upper left and right corners of the model to minimize numerical problems that can occur when boundary conditions are not specified.

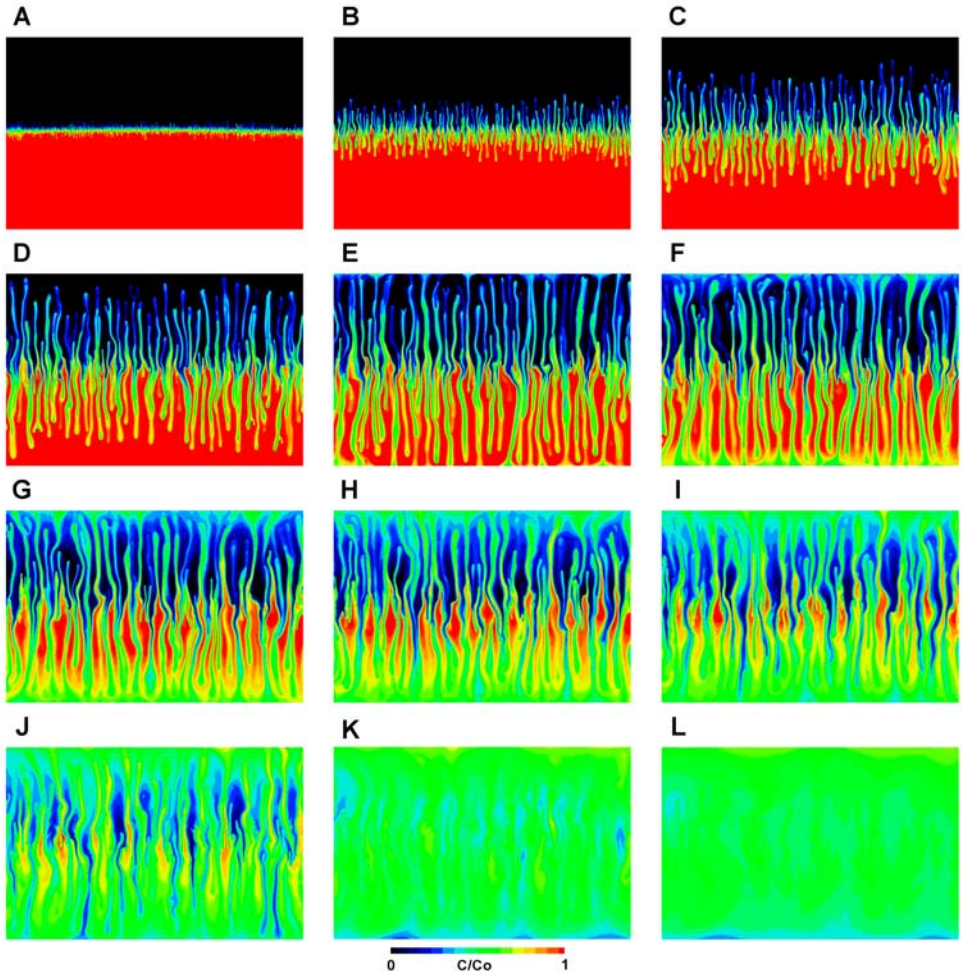

Figure 2. Observed results from *Pringle et al.* [2002] at (a) $t^* = 4.03 \times 10^{-5}$, (b) $t^* = 1.31 \times 10^{-4}$, (c) $t^* = 2.21 \times 10^{-4}$, (d) $t^* = 3.22 \times 10^{-4}$, (e) $t^* = 4.23 \times 10^{-4}$, (f) $t^* = 5.24 \times 10^{-4}$, (g) $t^* = 6.04 \times 10^{-4}$, and (h) $t^* = 7.25 \times 10^{-4}$, (i) $t^* = 7.85 \times 10^{-4}$, (j) $t^* = 1.03 \times 10^{-3}$, (k) $t^* = 1.77 \times 10^{-3}$, and (l) $t^* = 3.17 \times 10^{-3}$. Color sequence black-blue-green-yellow-orange-red depicts normalized dye concentrations from 0 to 1.

Specified-pressure boundary conditions are treated as pressure-dependent boundary conditions (Cauchy boundary condition) and solute mass is added to the model only if an inward gradient from the specified pressure boundary condition to the upper left or right nodes is calculated. No fluid inflow occurred during the simulation and only a small amount of fluid left the model through the specified pressure nodes (<2%).

[27] Although *Pringle et al.* [2002] indicated that significant effort was expended to minimize initial perturbations and the thickness of the initial solute interface was small (~0.001 m), some perturbations existed at the start of the experiment and were seeds for initial finger development. Model error (round-off error) can create perturbations that vary spatially and temporally in an uncontrollable fashion [*Simmons et al.*, 1999]. Small changes in dispersion parameters and spatial and temporal discretization can cause different perturbations to occur. To control initial seeds for finger development, random noise with a mean of zero and maximum amplitude of 0.5% of maximum initial concentrations was applied to the sodium chloride and sucrose concentrations at the initial solution interface. The sensitivity of model results to the magnitude and amplitude of perturbations was not evaluated in this study.

[28] To develop initial perturbations, two random numbers between 0 and 1 were generated for each node located at the initial solution interface (z = 0.08125 m). If the first random number (R_{N1}) was less than 0.5, then the sodium chloride concentration for the node was reduced by $0.01R_{N1}C_{NaCl}$(max), where C_{NaCl}(max) is the maximum initial sodium chloride concentration (Table 2). If the second random number (R_{N2}) was less than 0.5, then the sucrose concentration for the node was reduced by $0.01R_{N2}C_{Sucrose}$(max), where $C_{Sucrose}$(max) is the maximum initial sucrose concentration (Table 2). If either R_{N1} or R_{N2} was greater than or equal to 0.5, sodium chloride and/or sucrose concentrations for the node remained unchanged and equal to maximum values defined in Table 2. Initial dye concentrations at the interface were not perturbed. A consistent initial pressure field was developed using the perturbed concentration fields and the Hele-Shaw cell

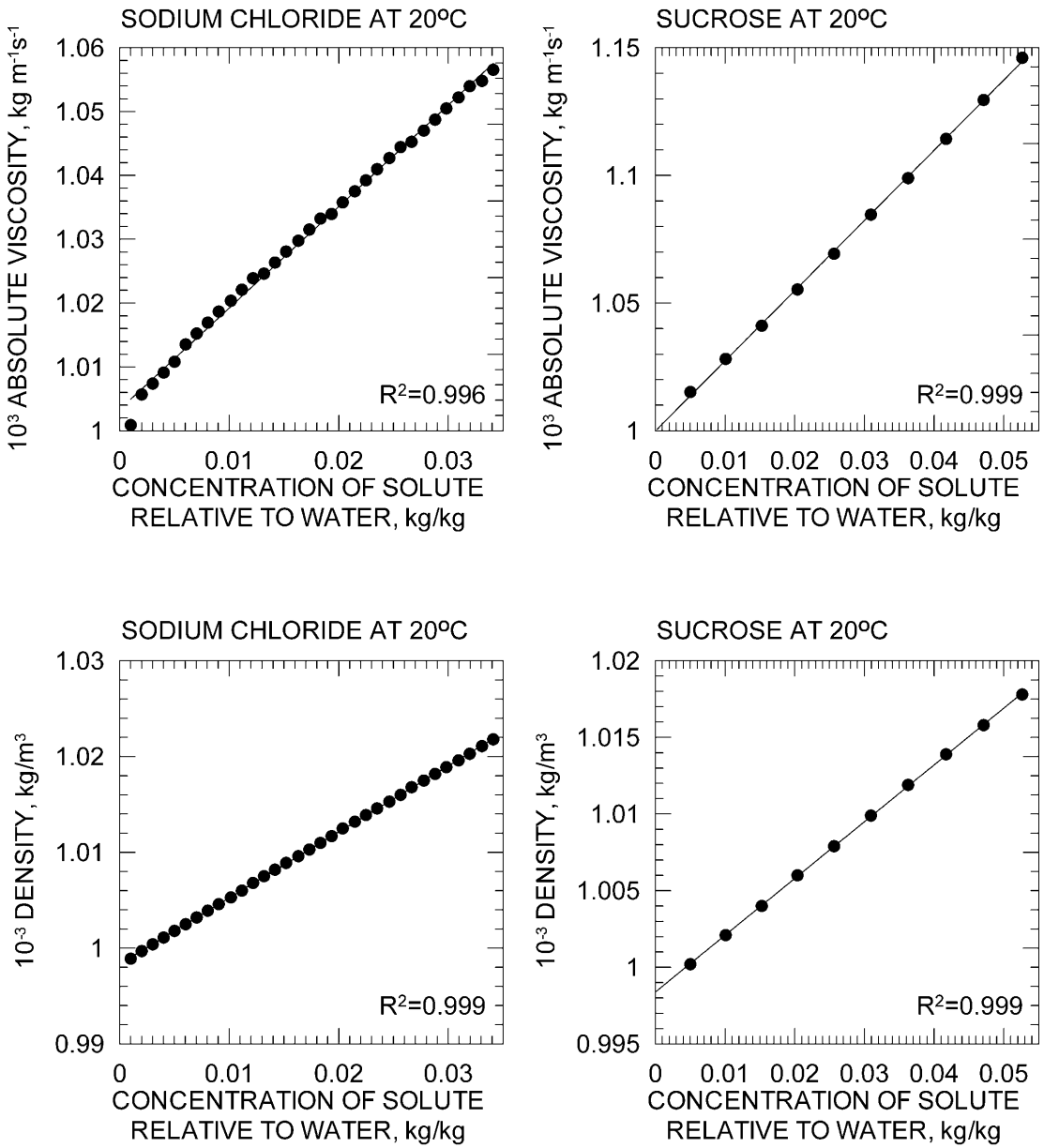

Figure 3. Absolute viscosity and fluid density relationships with sodium chloride and sucrose concentration used in all simulations. Data are from *Weast* [1986].

Table 3. Numerical Parameters Used

Parameter	Value
$\Delta x = \Delta y$	2.48×10^{-4} m
Number of elements in x direction	1024
Number of elements in z direction	656
Gravitational acceleration (g sin25°)	4.14 m/s^2
Porosity ε	1.0
Cell Thickness b	1.0 m
Base fluid density ρ_o	998.0 kg/m^3
Base fluid viscosity μ_o	1.00×10^{-3} kg/m s
Coefficient of fluid density change to sodium chloride concentration ($\partial\rho/\partial C_{NaCl}$)	689.0 kg_{fluid}^2/kg_{NaCl} m^3
Coefficient of fluid density change to sucrose concentration ($\partial\rho/\partial C_{Sucrose}$)	371.0 $kg_{fluid}^2/kg_{Sucrose}$ m^3
Coefficient of fluid density change to dye concentration ($\partial\rho/\partial C_{Dye}$)	0.00 kg_{fluid}^2/kg_{Dye} m^3
Coefficient of fluid viscosity change to sodium chloride concentration ($\partial\mu/\partial C_{NaCl}$)	1.59×10^{-3} kg_{fluid} kg/kg_{NaCl} m s
Coefficient of fluid viscosity change to sucrose concentration ($\partial\mu/\partial C_{Sucrose}$)	2.75×10^{-3} kg_{fluid} kg/kg_{NaCl} m s
Coefficient of fluid viscosity change to dye concentration ($\partial\mu/\partial C_{Dye}$)	0.00 kg_{fluid} kg/kg_{NaCl} m s
Longitudinal dispersivity α_L	0.00 m
Transverse dispersivity α_T	0.00 m

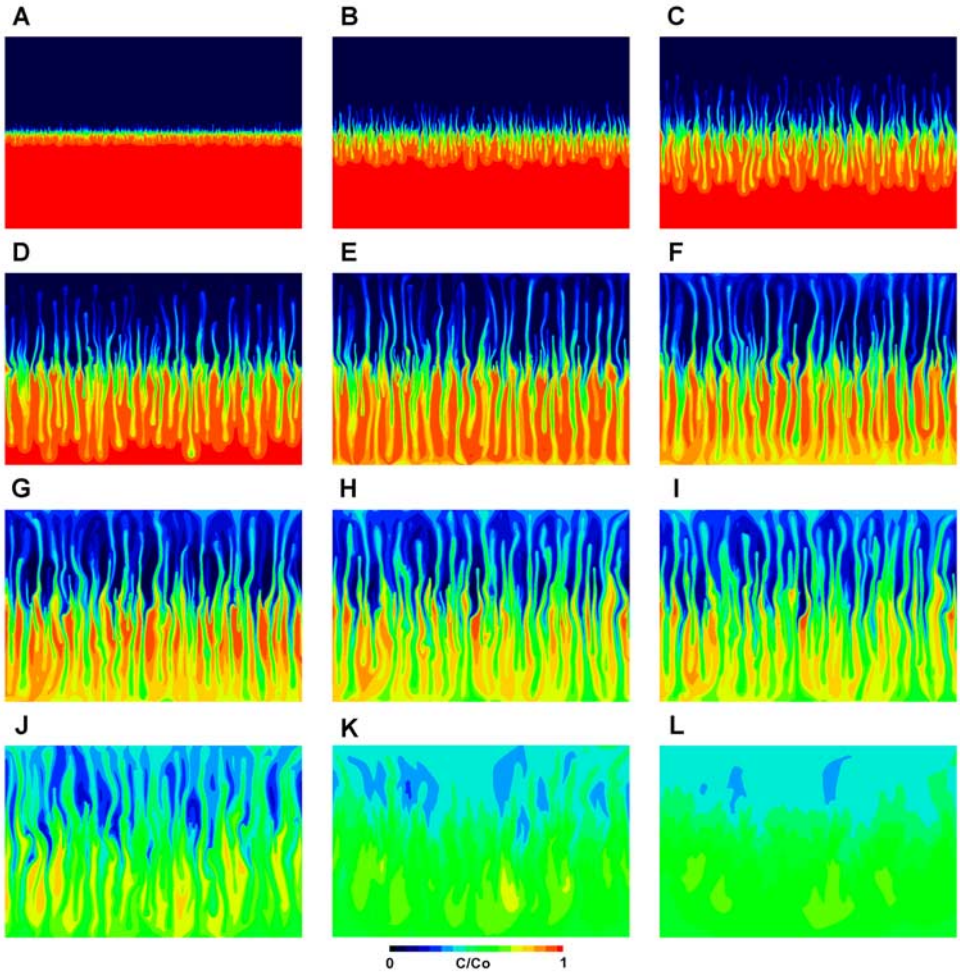

Figure 4. Simulated numerical results for the dye at (a) $t^* = 4.03 \times 10^{-5}$, (b) $t^* = 1.31 \times 10^{-4}$, (c) $t^* = 2.21 \times 10^{-4}$, (d) $t^* = 3.22 \times 10^{-4}$, (e) $t^* = 4.23 \times 10^{-4}$, (f) $t^* = 5.24 \times 10^{-4}$, (g) $t^* = 6.04 \times 10^{-4}$, and (h) $t^* = 7.25 \times 10^{-4}$, (i) $t^* = 7.85 \times 10^{-4}$, (j) $t^* = 1.03 \times 10^{-3}$, (k) $t^* = 1.77 \times 10^{-3}$, and (l) $t^* = 3.17 \times 10^{-3}$. Color sequence black-blue-green-yellow-orange-red depicts normalized dye concentration from 0 to 1.

experiment parameters and fluid parameters summarized in Tables 1–3.

6. Results and Discussion

6.1. Simulated Numerical Results

[29] Simulated numerical results at the same dimensionless times of *Pringle et al.* [2002] are shown in Figure 4. The concentrations shown in Figure 4 are simulated dye concentrations. Qualitatively, the numerical results are very similar to the experimental results until $t^* = 1.03 \times 10^{-3}$, although experimental vertical finger evolution appears to be slightly ahead of simulated fingers. *Pringle et al.* [2002] presented three measures that were used to quantitatively assess finger movement, vertical mass flux, and average horizontal finger width. The third measure can be applied to simulated results and used to determine the correspondence of finger development and evolution in the numerical model and the Hele-Shaw experiment. For the quantitative measures used to assess finger movement and vertical mass flux, dye concentration fields were horizontally averaged. Concentrations along a horizontal traverse of the Hele-Shaw cell were used to calculate average horizontal finger widths.

[30] The first quantitative measure is the normalized vertical length scale, $h^* = h/H$, which is a measure of evolving finger structure where h is the vertical distance in the plane of the Hele-Shaw cell between the horizontally averaged 0.05 and 0.95 dye concentration at time t^* and H is the height in the plane of the Hele-Shaw cell. Both h and h^* become undefined as fingers invert at their ends after reaching the top and bottom boundaries. The second quantitative measure is the normalized mass transfer of dye, $M^* = M/M_o$, upward across the centerline of the cell where M is the dye mass above the centerline of the cell at time t^* and M_o is the total dye mass in the cell. The third quantitative measure is the normalized horizontal length scale, $\lambda^* = \lambda/H$, along a horizontal traverse of the Hele-Shaw cell where λ is the average horizontal length scale and H is the height of the Hele-Shaw cell. The average horizontal length scale, λ, was determined by dividing the cell length by the number of upward and downward concentration pairs along a horizontal traverse of the cell.

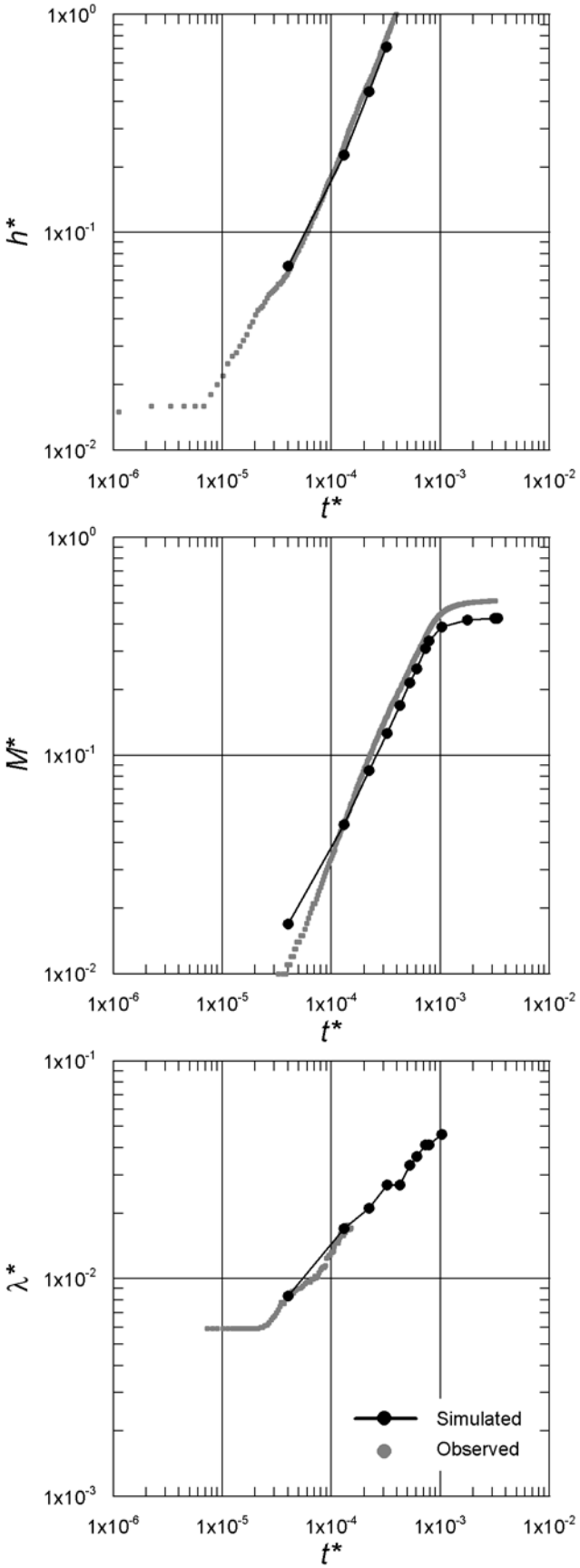

This measure can be thought of as twice the normalized average finger width or a normalized wavelength and will have different values at different vertical traverses. Differences in simulated and observed experimental values are presented as percent errors:

$$\%Error = 100\frac{(C_{sim} - C_{obs})}{C_{obs}} \tag{6}$$

where C_{sim} is the simulated concentration and C_{obs} is the observed experimental concentration. Positive percent errors indicate the model is oversimulating concentrations and negative percent errors indicate the model is undersimulating concentrations. Simulated data is available for all t^* values shown on Figure 4 and are used to calculated simulated h^*, M^*, and λ^* values.

[31] Comparison of simulated and observed values of h^*, M^*, and λ^* are shown in Figure 5. Observed values from all experimental images analyzed by *Pringle et al.* [2002] are presented. Simulated results were only saved at t^* values indicated in Figure 2 to minimize data storage requirements. In general, numerical results compare well to observed values of h^* at all compared times. h^* percent errors range from +6% at early times to −9% at late times and had an average value of −4% for all times compared.

[32] Numerical results compare reasonably well to observed values of M^* until $t^* = 1 \times 10^{-3}$. After $t^* = 1 \times 10^{-3}$, simulated mass transfer is less than observed mass transfer. M^* percent errors range from +53% at early times to −17% at late times and had an average value of −8% for all times compared. Large percent errors at early times are an artifact of small M^* values and represent small absolute differences in mass transfer (e.g., 0.011 observed and 0.017 simulated). Reduced simulated mass transfer is also evident in Figure 4l where fingers are more defined than in observed results (Figure 2l). More intense convection at late times would move additional mass vertically and would lead to better mixing of the sucrose and sodium chloride and reduction/elimination of the finger structure observed at late times in the simulated results.

[33] Simulated λ^* values compare well to observed values in the finger generation zone at the centerline of the cell during the mature stage of finger development. Only two simulated and observed λ^* values are coincident but λ^* percent errors range from ±1%. Temporally, the mature stage simulated λ^* exhibits a power law relationship with an exponent of 0.52 for $4.03 \times 10^{-5} \leq t^* \leq 1.03 \times 10^{-3}$. *Pringle et al.* [2002] did not present λ^* values for $t^* > 2.0 \times 10^{-4}$ because of the increasingly diffuse nature of the concentration swings in the finger generation zone resulted in inaccurate measurements. Simulated λ^* values for $t^* > 2.0 \times 10^{-4}$ are presented because they appear consistent

Figure 5. Normalized vertical length, $h^* = h/H$, mass transfer across the center line, $M^* = M/M_o$, and normalized horizontal length scale at the center line, $\lambda^* = \lambda/H$, as a function of time showing regions of steady growth for the original Hele-Shaw experiment (shaded circles) and the numerical simulation. Observed data included for all 300 images taken by *Pringle et al.* [2002] of the Hele-Shaw cell experiment.

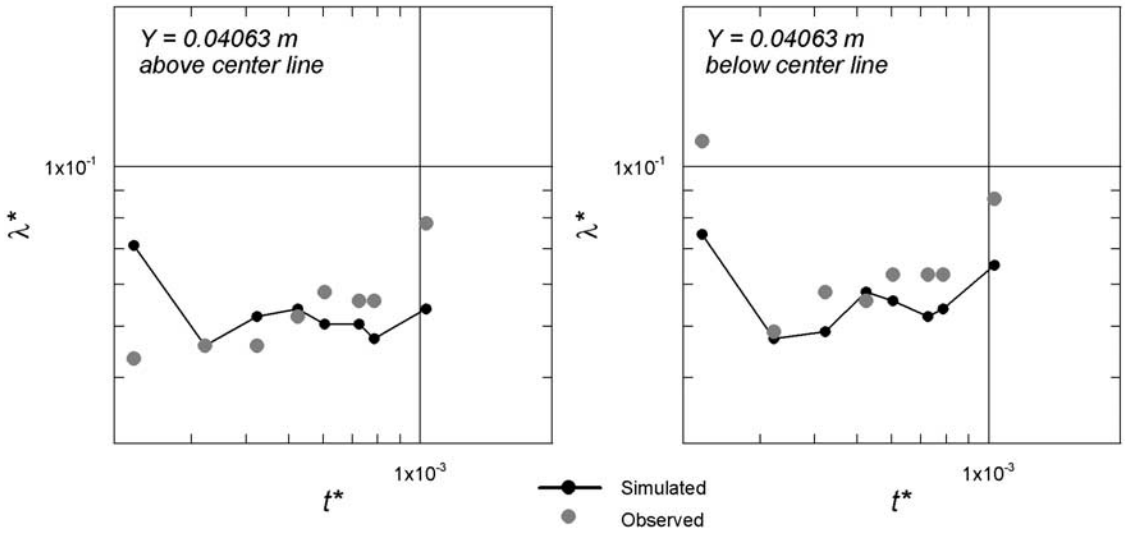

Figure 6. Normalized horizontal length scale, $\lambda^* = \lambda/H$, at 0.75H and 0.25H as a function of time showing apparent asymmetry in finger evolution above and below the center line for simulated and observed dye concentrations.

with mature stage λ^* data for t^* values less than 2.0×10^{-4}. The simulated power law exponent compares favorably well with the observed mature stage exponent of 0.57 and the experimental work of *Cooper et al.* [2001] which yielded an exponent of ~0.5.

[34] Visually, finger dimensions (vertical and horizontal lengths) below the centerline appear to be larger than finger dimensions above the centerline when observed and simulated dye concentrations on Figures 2 and 4 are compared, suggesting finger evolution is faster below the finger generation zone at the centerline. Differences in finger evolution above and below the centerline can be explained by the differences in the molecular diffusivity of sodium chloride and sucrose. Because the molecular diffusivity of sucrose is a factor of three less than sodium chloride, density instabilities below the centerline will gain sodium chloride mass at a much greater rate than sucrose mass is lost and density instabilities above the centerline will lose sodium chloride mass faster than sucrose mass is gained.

[35] To quantitatively evaluate vertical finger evolution away from the finger generation zone, simulated and observed λ^* values at $0.75H$ (y = 0.1219 m) and $0.25H$ (y = 0.0406 m) have been calculated and are shown in Figure 6. λ^* values are undefined for t^* values less than 2.21×10^{-4} because the fingers have not penetrated to $\pm 0.25H$ from the centerline. Because of the generally diffuse nature of the fingers during the mature and rundown stages, average λ^* values and average percent errors in simulated and observed values at $0.75H$ and $0.25H$ are compared. Furthermore, λ^* values have not been calculated for t^* values greater than 7.85×10^{-4} when there is significant lateral movement of solute at the top and bottom of the Hele-Shaw cell. Observed average λ^* values at $0.75H$ and $0.25H$ are 5.52×10^{-2} and 6.16×10^{-2} at t^* values greater than 3.2×10^{-4} and supports the qualitative assessment that finger evolution is greater below the centerline. Simulated average λ^* values at $0.75H$ and $0.25H$ are 5.05×10^{-2} and 5.42×10^{-2} at t^* values greater than 3.2×10^{-4} and indicate simulated finger evolution is faster below the centerline. Average percent errors in λ^* values at $0.75H$ and $0.25H$ at t^* values greater than 3.2×10^{-4} are -7% and -12%, respectively. It is suspected that reduced simulated finger evolution at $0.75H$ and $0.25H$ is a result of decreased vertical mass transfer rates in the numerical model. A possible explanation for decreased mass transfer rates is discussed below in the following section.

6.2. Influence of Discretization on Numerical Results

[36] Mass transfer resulting from double-diffusive flow is a function of density differences that are affected by finger dimensions. Because most mass transfer in a double-diffusive flow system is a result of convection, small finger dimensions may increase vertical mass transfer by allowing larger lateral and vertical density gradients to be maintained and permit more fingers to develop in a given lateral distance. Simulation of solute transport can often be difficult when truncation errors and/or grid size exceed the length scale of the concentration field being simulated. Truncation errors are commonly referred to as numerical dispersion and cause artificial spreading of concentration gradients. Numerical dispersion is a function of fluid velocity, element size, and the numerical technique used to solve the solute transport equation [*Lantz*, 1971]. When a centered in time (CIT) and center in space (CIS) numerical technique is used, no numerical dispersion is introduced, but dispersion, discretization, and time step lengths must be sufficient to satisfy Peclet and Courant number criteria and can be numerically expensive. When less expensive CIT-backward in space (BIS), backward in time (BIT)-CIS, or BIT-BIS numerical techniques are used numerical dispersion is $v_x\Delta x/2$, $v_x^2\Delta t/2$, and $v_x\Delta x/2 + v_x^2\Delta t/2$, respectively [*Lantz*, 1971; *Kipp*, 1987]. An implicit assumption in these equations is that a single element is smaller than the dimensions of any solute features of interest (i.e., solute fronts are larger than a single element). If solute fronts are less than a single element, minimum concentration front widths are $\Delta x/2$ regardless of the fluid velocity and the numerical technique used. This is particularly true for finite

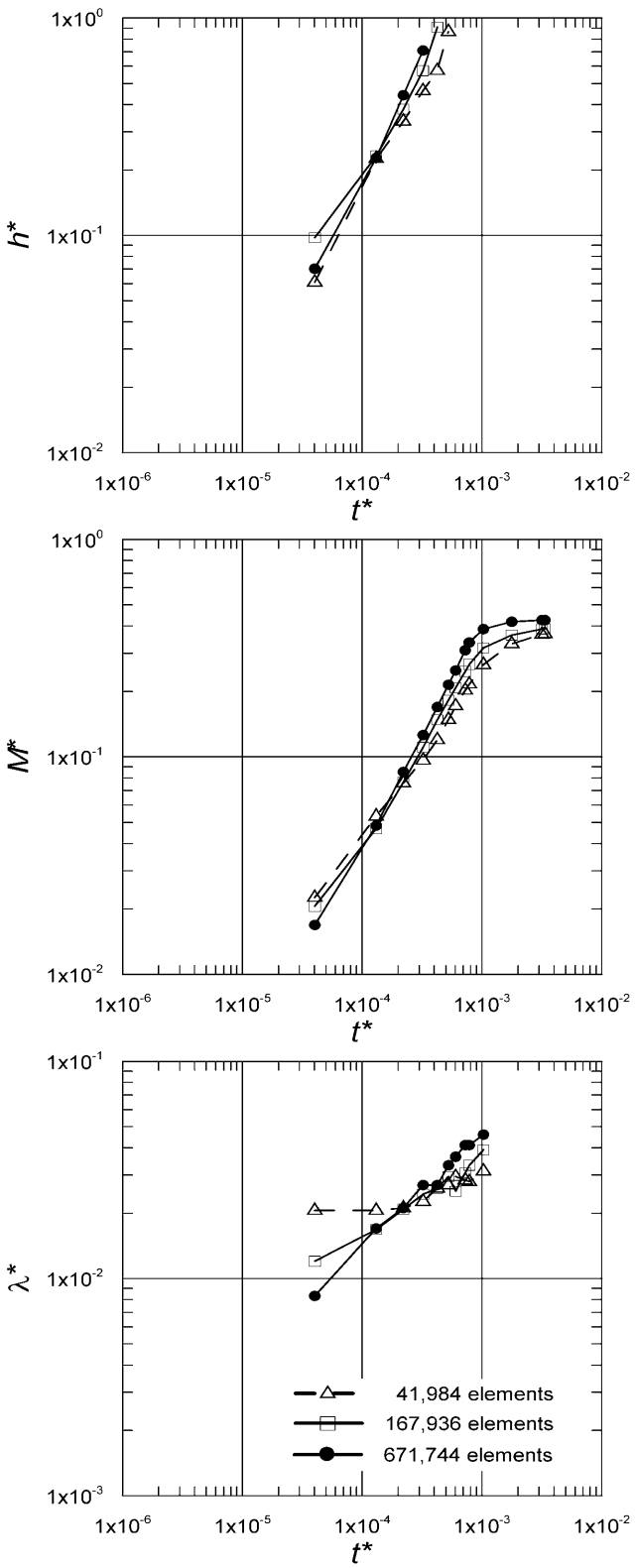

Figure 7. Normalized vertical length, $h^* = h/H$, mass transfer across the center line, $M^* = M/M_o$, and normalized horizontal length scale at the center line, $\lambda^* = \lambda/H$, as a function of time, showing regions of steady growth for the 41,984-, 167,936-, and 671,744-element simulations.

element codes that use linear basis functions to develop the matrix equations used to solve the flow and transport equations. A BIT-CIS numerical technique has been used in these numerical simulations and solute fronts (fingers) can be sharp relative to the element sizes used. As a result, the minimum finger width that can be resolved in these simulations is $\Delta x/2$.

[37] The finest spatial discretization used in the numerical simulations was a factor of 1.6 larger than the pixel size of the Hele-Shaw experiment and may not be sufficient to represent density gradients in the real system and resulting mass transfer. The effect of spatial discretization on simulated results was quantified using coarser discretizations of 41,984 and 167,936 elements (a factor of 16 and 4 fewer elements, respectively). The sides of the elements of the 41,984 and 167,936 element problems were 4.96×10^{-4} m and 9.92×10^{-4} m, respectively.

[38] Comparison of h^*, M^*, and λ^* values for the 41,984-, 167,936-, and 671,744-element simulations are shown on in Figure 7. Comparison of h^*, M^* and λ^* values for the three levels of discretization shows that normalized length scales, mass transfer, and normalized horizontal length scales are a function of element size.

[39] The percent error of h^* values for the 41,984-element simulation was -8% at early times to -41% at late times and had an average of -22%. The percent error of M^* values for the 41,984-element simulation ranged from $+105\%$ at early times to -28% at late times and had an average value of -21%. The percent error of λ^* values for the 41,984-element simulation ranged from $+146\%$ to $+23\%$.

[40] The percent error of h^* values for the 167,936-element simulation was $+48\%$ at early times to -27% at late times and had an average of -1%. The percent error of M^* values for the 167,936-element simulation ranged from $+87\%$ at early times to -24% at late times and had an average of -16%. The percent error of λ^* values for the 167,936-element simulation ranged from $+44\%$ to $+0\%$.

[41] Percent errors were calculated in all comparisons using equation (6) and simulated and observed experimental values. Large percent differences at early times are a result of small values of h^* and M^* and represent relatively small differences in the normalized length scale and normalized mass transfer.

[42] These results suggest that coarser discretization and subsequently coarser fingers move more mass vertically at early stages of finger development, but after $t^* \approx 2 \times 10^{-4}$ (mature finger stage) fingers are less defined both horizontally and vertically as a result of numerical dispersion and are unable to induce as much vertical mass transfer (as simulated in the 671,744-element simulation and in the observed in the Hele-Shaw experiment). Enhanced mass transfer in the early stages of finger development is likely a result of initial perturbations that are effectively more concentrated at a coarser discretization, resulting in larger areas of density contrast at the solution interface. These results also suggest that a mesh with more than 671,744 elements would likely result in simulated normalized length scales and mass transfer closer to values calculated for the Hele-Shaw experiment. During the course of this study it was determined that it was not feasible to reduce the grid size by a factor of two (2) because of the

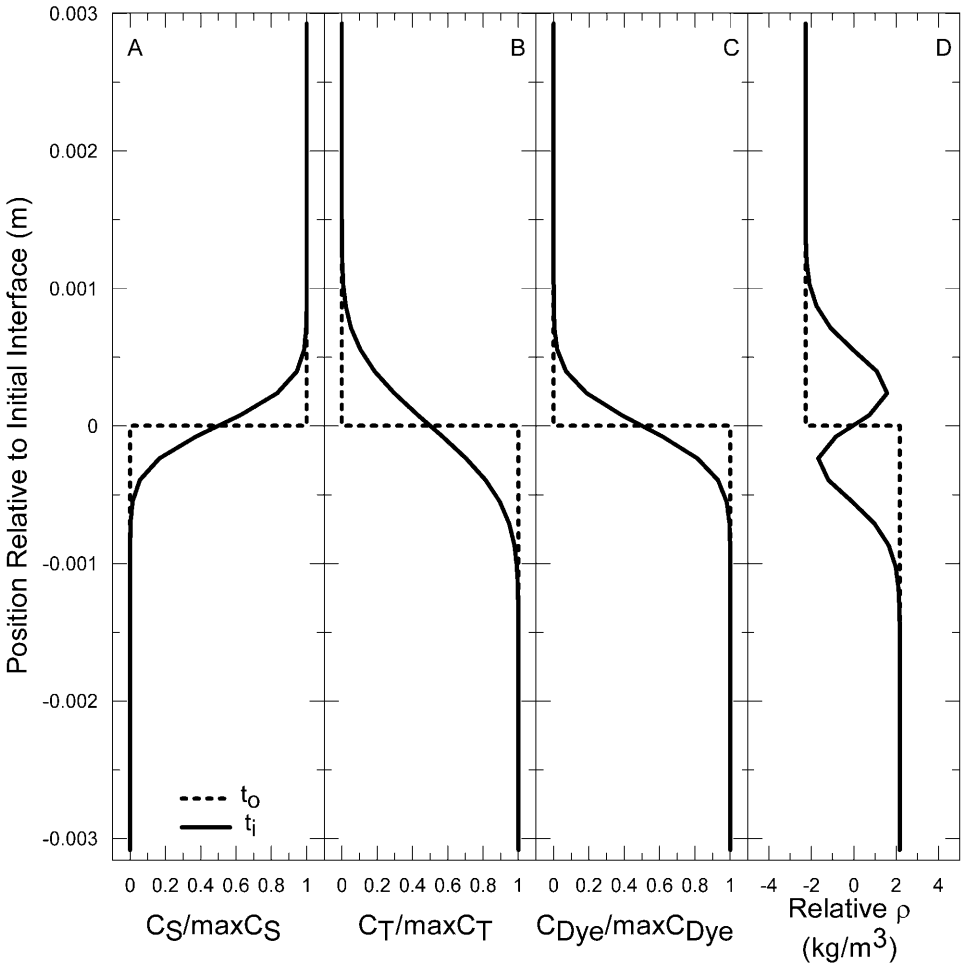

Figure 8. Conceptual (a) sucrose concentrations, (b) sodium chloride concentrations, (c) dye concentrations, and (d) fluid density relative to the initial average fluid density showing the effect of different diffusivities on component concentrations and fluid density. Concentrations calculated at time t_i using a one-dimensional form of the diffusion equation with diffusivities and spatial dimensions consistent with the Hele-Shaw experimental setup. Note that part of the vertical density profile is unstable at time t_0.

resulting excessive run times and RAM requirements of ~28 days and ~3.8 GB for a 2,686,976 element mesh, respectively, for such a simulation.

6.3. Comparison of the Diffusion Rates of Dye, Sodium Chloride, and Sucrose

[43] The molecular diffusivity of sodium chloride is a factor of 2.5 larger than the molecular diffusivity of the dye used to visualize sodium chloride concentrations. Similarly, the molecular diffusivity of sodium chloride is a factor of 3.0 larger than the molecular diffusivity of sucrose. The effects of the different molecular diffusivities on normalized sodium chloride, sucrose, and the dye concentrations and the resulting density profile relative to average initial column densities in a one-dimensional column are shown graphically on Figure 8. The curves shown on Figure 8 at time t_o and t_i represent the initial vertical profiles and vertical profiles after some period of time using a one-dimensional form of the diffusion equation that assumes diffusion is Fickian, does not account for the effect of vertical fluid-density differences on fluid flow, uses fluid parameters identical to the original experiment (Table 2), and spatial dimensions similar to the Hele-Shaw experiment.

[44] As shown in Figure 8, sodium chloride diffuses upward faster than sucrose diffuses downward from the initially stable density configuration. This difference in diffusion rates causes the development of instabilities in fluid density (Figure 8d) that will initiate convection when the destabilizing buoyancy forces exceed the stabilizing effects of diffusion. Convection will continue until diffusion of sodium chloride (the destabilizing component) eliminates density instabilities/gradients and/or fingers reach the top and bottom boundaries of the Hele-Shaw cell. Mass transfer typically decreases once fingers reach the top and bottom boundaries of the Hele-Shaw cell unless the horizontal length scale is relatively large and subsequent horizontal mass transfer rates are high.

[45] Vertical fluid flow caused by density instabilities will transport fluid with and without dye upward and downward, respectively, but differences in the molecular diffusivities of sodium chloride and dye will cause imperfect mapping of chloride concentrations by the dye. The discrepancy

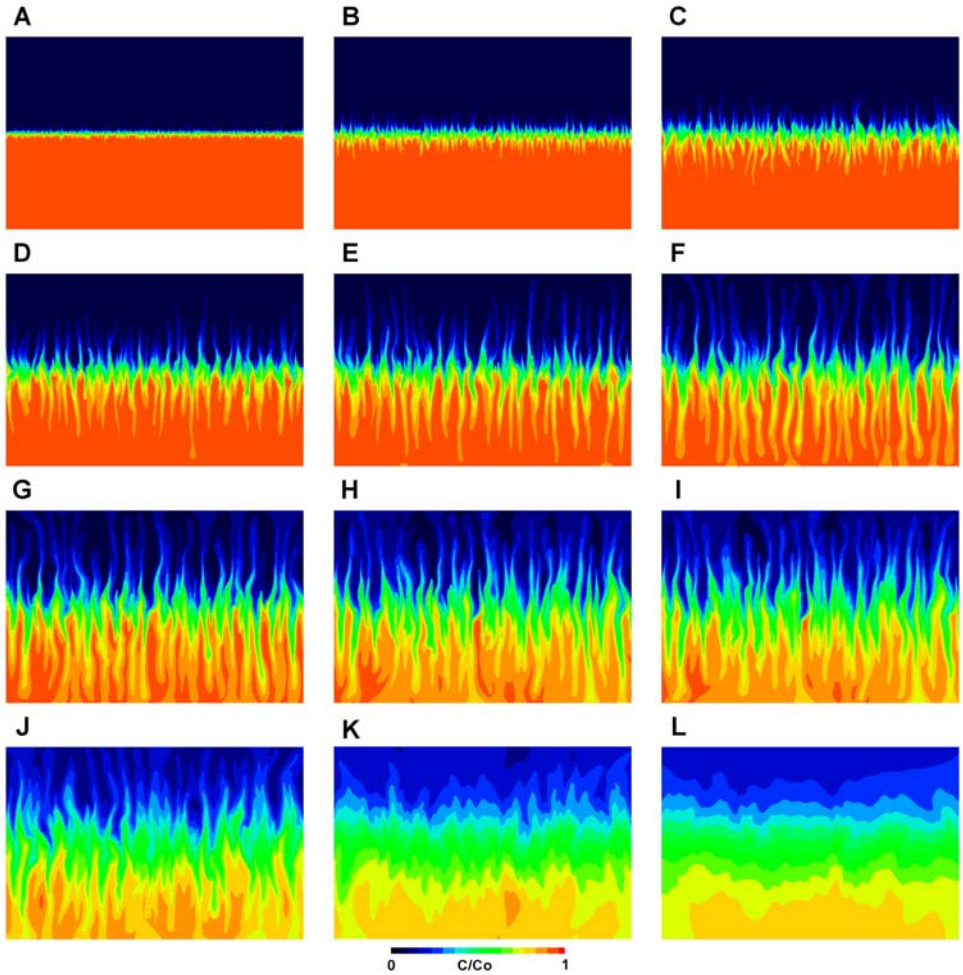

Figure 9. Simulated numerical results for sodium chloride at (a) $t^* = 4.03 \times 10^{-5}$, (b) $t^* = 1.31 \times 10^{-4}$, (c) $t^* = 2.21 \times 10^{-4}$, (d) $t^* = 3.22 \times 10^{-4}$, (e) $t^* = 4.23 \times 10^{-4}$, (f) $t^* = 5.24 \times 10^{-4}$, (g) $t^* = 6.04 \times 10^{-4}$, and (h) $t^* = 7.25 \times 10^{-4}$, (i) $t^* = 7.85 \times 10^{-4}$, (j) $t^* = 1.03 \times 10^{-3}$, (k) $t^* = 1.77 \times 10^{-3}$, and (l) $t^* = 3.17 \times 10^{-3}$. Color sequence black-blue-green-yellow-orange-red depicts normalized sodium chloride concentration from 0 to 1.

between sodium chloride and dye concentrations will increase as the simulation progresses as differences in mass diffusion increase and may significantly affect calculated quantitative measures of finger development and vertical mass transfer. Furthermore, dye concentrations should map the downward movement of sucrose better than the upward movement of sodium chloride because of the similarity of the molecular diffusivities of sucrose and dye (Figures 8a and 8c). Unlike the Hele-Shaw experiment where sodium chloride and sucrose concentrations are not available independent of observed dye concentrations, the numerical model allows qualitative and quantitative comparisons of sodium chloride, sucrose, and dye concentrations.

[46] Figure 9 shows simulated sodium chloride concentrations at the same t^* values evaluated in Figure 4. Figure 10 shows normalized sodium chloride, sucrose, and dye concentrations at $t^* = 5.24 \times 10^{-4}$, $t^* = 7.85 \times 10^{-4}$, and $t^* = 3.17 \times 10^{-3}$. Fluid density at $t^* = 5.24 \times 10^{-4}$, $t^* = 7.85 \times 10^{-4}$, and $t^* = 3.17 \times 10^{-3}$ are also shown on Figure 10. In general, sodium chloride concentrations are horizontally more dispersed (wider) than simulated dye concentrations (Figure 4) and visually it appears that vertical mass transfer of sodium chloride is less than that of the dye. Sucrose concentrations appear to map the inverse of dye concentrations reasonably well and exhibit similar finger lengths and widths. Development of a stable density configuration as the system transitions from a mature stage when convection is active to a rundown stage when diffusion dominates is shown on Figures 10j–10l.

[47] Comparison of the vertical length scales (h^*), vertical mass transfer (M^*), and normalized horizontal length scales (λ^*) of dye and sodium chloride are shown in Figure 11. Vertical length scales (h^*) vertical mass transfer (M^*), and normalized horizontal length scales (λ^*) have not been calculated for sucrose because these measures were not calculated by *Pringle et al.* [2002] because of the inability to measure sucrose concentrations. Percent errors for h^* values for sodium chloride ranged from −19% at early times to −46% at late times and averaged −36% of experimental dye values. Percent error for M^* values for sodium chloride were +25% at early times to −41% at late times and averaged −35% of experimental dye values. The percent error of λ^* values for the 167,936 element simulation ranged from +14% to +7% when compared to experimental dye values.

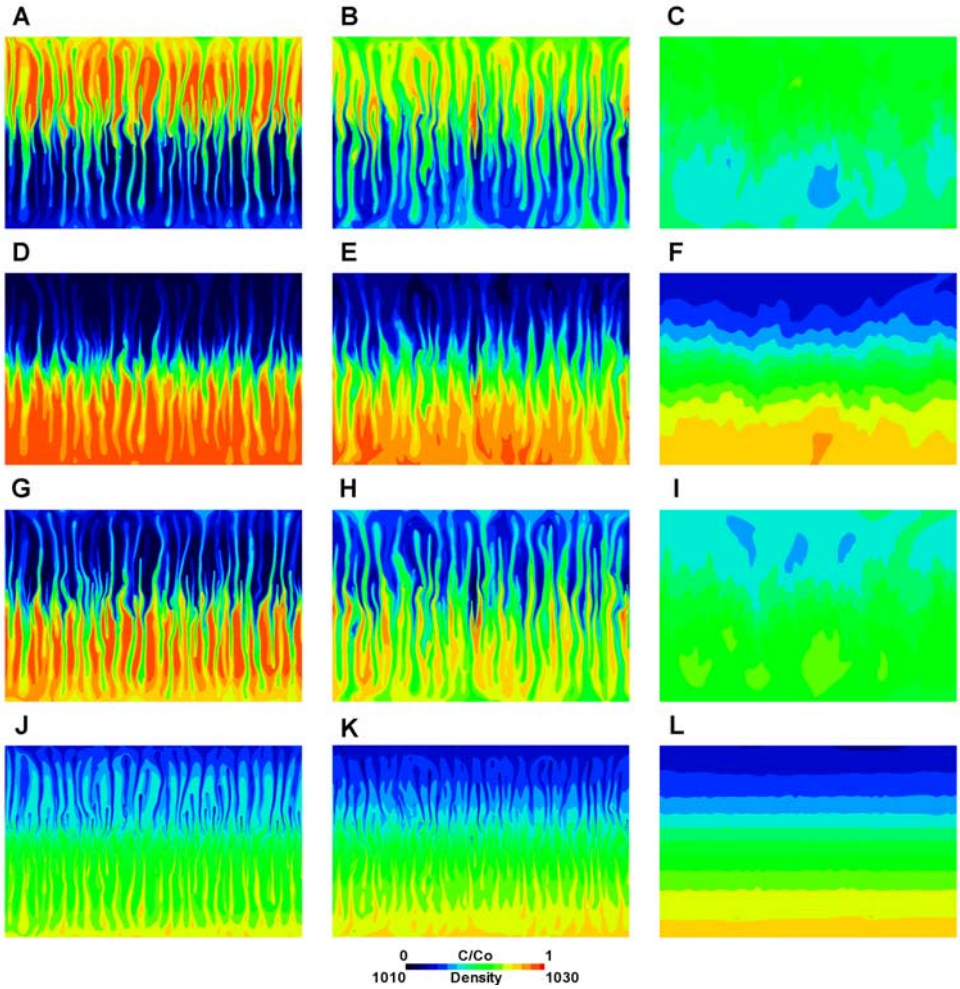

Figure 10. Simulated sucrose concentrations at (a) $t^* = 5.24 \times 10^{-4}$, (b) $t^* = 7.85 \times 10^{-4}$, and (c) $t^* = 3.17 \times 10^{-3}$. Simulated sodium chloride concentrations at (d) $t^* = 5.24 \times 10^{-4}$, (e) $t^* = 7.85 \times 10^{-4}$, and (f) $t^* = 3.17 \times 10^{-3}$. Simulated dye concentrations at (g) $t^* = 5.24 \times 10^{-4}$, (h) $t^* = 7.85 \times 10^{-4}$, and (i) $t^* = 3.17 \times 10^{-3}$. Simulated fluid density at (j) $t^* = 5.24 \times 10^{-4}$, (k) $t^* = 7.85 \times 10^{-4}$, and (l) $t^* = 3.17 \times 10^{-3}$. Color sequence black-blue-green-yellow-orange-red depicts normalized concentrations from 0 to 1 (Figures 10a–10i) and fluid density (Figures 10j–10l).

Calculated h^* and M^* values for sodium chloride were less than calculated dye values at 16 out of 17 values of t^* compared and had a difference in average h^* and M^* values of −32% and −27%, respectively. In all comparisons, percent errors were calculated using equation (6) and simulated and observed experimental values.

[48] Increased discrepancies between sodium chloride and dye concentrations over the length of the experiment were noted by *Pringle et al.* [2002] and were attributed to the dominance of diffusion in the rundown stages of the experiment ($t^* \geq 9.00 \times 10^{-4}$) and interaction of sodium chloride, sucrose, and dye. The maximum error caused by using the dye to map sodium chloride was estimated by *Pringle et al.* [2002] for the end of the experiment to be 5%, which is significantly less than that indicated using the numerical model.

7. Concluding Remarks

[49] The numerical model presented is capable of simulating high-resolution Hele-Shaw double-diffusive finger convection. The numerical model does a reasonable job of simulating the temporal and spatial evolution of convection except at late times ($t^* \geq 3.19 \times 10^{-3}$). Average percent errors in normalized vertical length scales (h^*) and normalized mass transfer (M^*) are less than 10% over the length of the simulation. At late times, simulated fingers remained more defined than were observed during the experiment and simulated mass transfer was a maximum of 8% less than observed.

[50] Numerical results are very sensitive to discretization and are closest to experimental results using elements that are 2.48×10^{-4} m along each side. Mass transfer was enhanced at early times and reduced at late times using meshes coarser than 2.48×10^{-4} m. Enhanced mass transfer at early times was a result of effectively larger initial instabilities (fewer nodes over the same length). Reduced mass transfer at late times was a result of increased lateral numerical dispersion. The finest discretization used was a factor of 1.6 larger than the resolution of experimental results and discretization sensitivity results suggest that numerical results would likely improve if cell sizes were

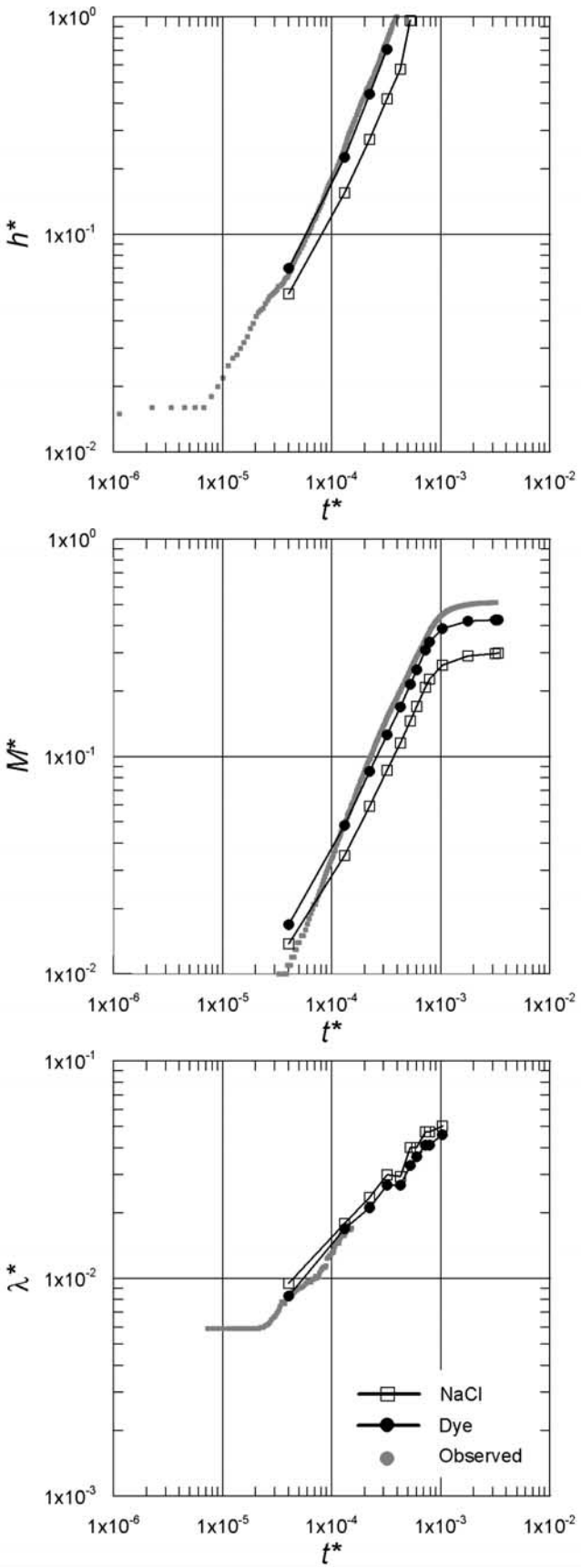

significantly smaller than the average finger width. Finer discretization was not attempted in this study because of excessive RAM requirements (>3 GB) and run times ($\gg$7 days) required to satisfy numerical stability requirements. Parallelization of the model code may be necessary to make simulations with finer meshes practical at this time.

[51] Differences in the molecular diffusivity of sodium chloride and the dye used to visualize sodium chloride concentrations result in an average difference of 27% in calculated dye and sodium chloride vertical mass transfer over the entire simulation length. The effect of differences in fluid properties could not be addressed in the experimental results because sodium chloride concentrations in the convection system could not be determined independent of dye concentrations.

[52] Comparison of the numerical model to experimental Hele-Shaw data is a robust test of the model's ability to simulate multicomponent variable density (double-diffusive) flow because the convective system is complex and driven exclusively by differences in fluid properties. These simulated results suggest it would also be possible in the future to apply the numerical model to additional Hele-Shaw double-diffusive convection data sets [e.g., *Cooper et al.*, 2001] with different buoyancy ratios (R_ρ).

Appendix A

[53] The hybrid weighted-residual and integrated finite difference method applied to the fluid mass balance (1) results in *NN* relations:

$$\sum_{j=1}^{NN}\left[\left(\frac{AF_i^{n+1}\delta_{ij}}{\Delta t^{n+1}}\right)+BF_{ij}^{n+1}+\nu_{pi}\delta_{ij}\right]p_j^{n+1} = Q_i^{n+1}+\nu_{pi}p_{BC_i}^{n+1}+DF_i^{(n+1)*}+\left(\frac{AF_i^{n+1}}{\Delta t^{n+1}}\right)p_i^n + \sum_{k=1}^{NS}\left[\left(CF_i^{n+1}\right)\left(\frac{dU_{ik}}{dt}\right)^n\right] \quad i=\overline{1,NN} \tag{A1a}$$

where δ_{ij} is the Kronecker delta, *NN* is the number of nodes in the finite element mesh, ν_{pi} is the pressure-based conductance for the specified pressure source in cell i, terms with the superscript *n* are at the end of the last time step, terms with the superscript $n+1$ are at the end of the current time step, and AF_i^{n+1}, BF_i^{n+1}, CF_i^{n+1}, and DF_i^{n+1} are matrices given by the following:

$$AF_i^{n+1}=(\rho((1-\varepsilon)\alpha+\varepsilon\beta))_i V_i \tag{A1b}$$

$$CF_i^{n+1}=\left(\varepsilon\frac{\partial\rho}{\partial U_k}\right)V_i \tag{A1c}$$

$$BF_{ij}^{n+1}=\int_V\left\{\left[\langle\langle\mathbf{k}^L\rangle\rangle\left(\frac{\rho}{\mu}\right)\cdot\nabla\phi_j\right]\right\}\cdot dV \tag{A1d}$$

Figure 11. Normalized vertical length, $h^* = h/H$, mass transfer across the center line, $M^* = M/M_o$, and normalized horizontal length scale at the center line, $\lambda^* = \lambda/H$, as a function of time showing regions of steady growth for the experimental dye concentrations, simulated sodium chloride concentrations, and simulated dye concentrations.

$$DF_i^{(n+1)*} = \int_V \left\{ \left[\langle\langle \mathbf{k}^L \rangle\rangle \left(\frac{\rho}{\mu} \right) \cdot \langle\langle \rho \mathbf{g} \rangle\rangle^* \right] \right\} \cdot dV \qquad \text{(A1e)}$$

where V_i is the volume of cell i, ϕ_j is the symmetric basis function in global coordinates for node j, $\langle\langle \mathbf{k}^L \rangle\rangle$ is the intrinsic permeability tensor, and $\langle\langle \rho \mathbf{g} \rangle\rangle^*$ is a discretization of $(\rho \mathbf{g})$ that is consistent with the discretization of ∇p. Consistent discretization of $(\rho \mathbf{g})$ relative to the discretization of ∇p is required to eliminate numerical dispersion of sharp concentration fronts in variable density fluids [*Voss and Souza*, 1987].

[54] The hybrid weighted-residual and integrated finite difference method applied to the fluid mass balance (1) results in *NN* relations for each simulated species:

$$\left\{ \begin{array}{l} \sum_{j=1}^{NN} \left[\left(\frac{AT_{ik}^{n+1} \delta_{ij}}{\Delta t^{n+1}} \right) + DT_{ijk}^{(n+1)*} + BT_{ijk}^{n+1} + \left[\nu_{U_{ik}} + \left(Q_i^{n+1} + Q_{BC_i}^n \right) c_w \right] \delta_{ij} \right] U_{jk}^{n+1} \\ = c_{wk} \left(Q_i^{n+1} U_{ik}^{(n+1)*} + Q_{BC_i}^n U_{BC_{ik}}^{n+1} \right) + \nu_{U_{ik}} U_{UBC_{ik}}^{n+1} + \Psi_{IN_{ik}}^{n+1} \\ + \left(\frac{AT_{ik}^{n+1}}{\Delta t^{n+1}} \right) U_{ik}^n \quad \mathrm{i} = \overline{1, \mathrm{NN}} \end{array} \right\} \mathrm{k} = \overline{1, \mathrm{NS}} \qquad \text{(A2a)}$$

where δ_{ij} is the Kronecker delta; *NN* is the number of nodes in the finite element mesh; *NS* is the number of simulate species; ν_{Uik} is the concentration-based conductance for the specified solute source in cell i; U_{ik} is the concentration of species k in cell i; $Q_{BC_i}^n$ is the mass of species k to cell i provided by a specified fluid source, for the previous time step; $U_{BC_{ik}}^{n+1}$ is the specified concentration of species k in cell i; terms with the superscript *n* are at the end of the last time step; and terms with the superscript $n + 1$ are at the end of the current time step. AT_i^{n+1}, BT_i^{n+1}, DT_i^{n+1}, and $\Psi_{IN_{ik}}{}^{n+1}$ are matrices given by

$$AT_{ik}^{n+1} = (\varepsilon \rho c_{wk})_i V_i \qquad \text{(A2b)}$$

$$DT_{ijk}^{(n+1)*} = \int_V \left[\langle\langle \varepsilon \rangle\rangle \rho c_{wk} \langle\langle \mathbf{v} \rangle\rangle^* \cdot \nabla \phi_j \right] dV \qquad \text{(A2c)}$$

$$BT_{ijk}^{n+1} = \int_V \left\{ \rho c_{wk} \left[\langle\langle \varepsilon \rangle\rangle (\sigma_{wk} \mathbf{I} + \langle\langle \mathbf{D}_k \rangle\rangle) \right] \cdot \nabla \phi_j \right\} \cdot \nabla \phi_i dV \qquad \text{(A2d)}$$

$$\Psi_{IN_{ik}}^{n+1} = \int_\Gamma \langle\langle \rho c_w [\varepsilon c_w (\sigma_{wk} \mathbf{I} + \mathbf{D}_k)] \cdot \nabla U \rangle\rangle^{n+1} \cdot \mathbf{n} \phi_i d\Gamma \qquad \text{(A2e)}$$

where V_i is the volume of cell i, ϕ_j is the symmetric basis function in global coordinates for node j, $\langle\langle \varepsilon \rangle\rangle$ is a element-wise discretization of porosity, $\langle\langle \mathbf{v} \rangle\rangle^*$ is a discretization of velocity that is consistent with the discretization of ∇p, $\mathbf{n}$ is the unit outward normal vector, and Γ is the external boundary area of the simulated region.

[55] Time derivatives are discretized using a backward finite difference approximation having the general form

$$\frac{d\gamma_i}{dt} = \frac{\gamma_i^{n+1} - \gamma_i^n}{t^{n+1} - t^n} \qquad \text{(A3)}$$

where γ_i can be the pressure or concentration of a simulated species at node i.

[56] Integration of terms in the fluid and solute mass balance equations are calculated on an element by element basis after transforming the quadrilateral element to a local coordinate system in which each element is a square in two dimensions or a cube in three dimensions. The numerical Gauss integration uses 2^d Gauss points in the local coordinate system where *d* is the spatial dimension of the problem (2-D or 3-D). Integration is only performed on the terms in the fluid mass balance and solute mass balance equations that are discretized in an element-wise fashion.

[57] The matrix systems for fluid flow (A1a) and multi-species transport (A2a) are linked by the fluid density (2), fluid viscosity (3), and fluid velocity (4). The density and viscosity coupling makes double-diffusive problems nonlinear. The degree of nonlinearity is dependent on buoyancy effects.

[58] To efficiently solve large two and three-dimensional problems, robust iterative solvers, which use efficient matrix storage methods, have been included in the model for solution of the flow and transport equations. Iterative methods that have been included include the generalized minimum residual (GMRES) and ORTHOMIN method with incomplete LU preconditioning.

[59] A sequential solution procedure for fluid flow and transport and an implicit Picard iterative scheme is used. Time extrapolation formulas based on initial values or values from the previous time step are used to extrapolate nodal values of pressure and concentration at the end of the current time step. To eliminate the need to specify a time step that is less than or equal to the minimum value required for convergence of all time steps in a numerical simulation, an automatic time step algorithm is used to reduce time step lengths when the prescribed number of iterations is exceeded.

[60] **Acknowledgments.** Partial funding for this research was provided by the U.S. Geological Survey Office of Groundwater. A special thanks to Scott Pringle for providing the experimental Hele-Shaw data and Alden Provost for fruitful discussions and comments that significantly improved earlier versions of the manuscript. We also gratefully acknowledge Stephen Gingerich and three anonymous reviewers for their constructive criticism of the manuscript.

References

Bear, J. (1979), *Hydraulics of Groundwater*, 567 pp., McGraw-Hill, New York.

Bear, J. (1988), *Dynamics of Fluids in Porous Media*, 764 pp., Dover, Mineola, N. Y.

Cooper, C. A., R. J. Glass, and S. W. Tyler (1997), Experimental investigation of the stability boundary for double-diffusive finger convection in a Hele-Shaw cell, *Water Resour. Res.*, *33*(4), 517–526.

Cooper, C. A., R. J. Glass, and S. W. Tyler (2001), The effects of buoyancy ratio on the development of double-diffusive finger convection in a Hele-Shaw cell, *Water Resour. Res.*, *37*(9), 2323–2332.

Detwiler, R. L., H. Rajaram, and R. J. Glass (2000), Solute transport in variable-aperture fractures: An investigation of the relative importance of Taylor dispersion and macrodispersion, *Water Resour. Res.*, *36*(7), 1611–1625.

Green, T. (1984), Scales for double-diffusive fingering in porous media, *Water Resour. Res.*, *20*, 1225–1229.

Hughes, J. D., and W. E. Sanford (2004), SUTRA-MS: A version of SUTRA modified to simulate heat and multiple-species solute transport, *U.S. Geol. Surv. Open File Rep., 2004-1207*, 141 pp.

Imhoff, P. T., and T. Green (1988), Experimental investigation of double-diffusive groundwater fingers, *J. Fluid Mech.*, *188*, 363–382.

Kazmierczak, M., and D. Poulikakos (1989), Transient double-diffusive convection experiments in a horizontal fluid layer extending over a bed of spheres, *Phys. Fluids A*, *1*(3), 480–489.

Kipp, K. L. (1987), HST3D: A computer code for simulation of heat and solute transport in three-dimensional ground-water flow systems, *U.S. Geol. Surv. Water Resour. Invest. Rep., 86-4095*, 517 pp.

Lambert, R. B., and J. W. Demenkow (1971), On the vertical transport due to fingers in double diffusive convection, *J. Fluid Mech.*, *54*, 627–640.

Lantz, R. B. (1971), Quantitative evaluation of numerical diffusion (truncation error), *Trans. Soc. Min. Eng. AIME*, *251*, 315–320.

Nield, D. A. (1968), Onset of thermohaline convection in a porous medium, *Water Resour. Res.*, *4*, 553–560.

Nield, D. A., and A. Bejan (1998), *Convection in Porous media*, 2nd ed., 496 pp., Springer-Verlag, New York.

Pringle, S. E., R. J. Glass, and C. A. Cooper (2002), Double-diffusive finger convection in a Hele-Shaw cell: An experiment exploring the evolution of concentration fields, length scales and mass transfer, *Transp. Porous Media*, *47*(2), 195–214.

Simmons, C. T., K. A. Narayan, and R. A. Wooding (1999), On a test case for density-dependent groundwater flow and solute transport models: The salt lake problem, *Water Resour. Res.*, *35*, 3607–3620.

Sorak, S., and G. F. Pinder (1999), Survey of computer codes and case histories, in *Seawater Intrusion in Coastal Aquifers—Concepts, Methods, and Practices*, edited by J. Bear et al., pp. 399–462, Kluwer Acad., Norwell, Mass.

Turner, J. S. (1967), Salt fingers across a density interface, *Deep Sea Res.*, *14*, 599–611.

Voss, C. I., and A. M. Provos (2002), SUTRA—A model for saturated-unsaturated, variable-density ground-water flow with solute or energy transport, *U.S. Geol. Surv. Water Resour. Invest. Rep., 02-4231*, 260 pp.

Voss, C. I., and W. R. Souza (1987), Variable density flow and solute transport simulation of regional aquifers containing a narrow freshwater-saltwater transition zone, *Water Resour. Res.*, *23*, 1851–1866.

Weast, R. C. (Ed.) (1986), *CRC Handbook of Chemistry and Physics*, 66th ed., CRC Press, Boca Raton, Fla.

J. D. Hughes and H. L. Vacher, Department of Geology, University of South Florida, 4202 E. Fowler Avenue, Tampa, FL 33620, USA. (jdhughe2@mail.usf.edu; vacher@chuma1.cas.usf.edu)

W. E. Sanford, U.S. Geological Survey, 12201 Sunrise Valley Drive, MS 431, Reston, VA 20192, USA. (wsanford@usgs.gov)